Hindawi Publishing Corporation
International Journal of Inorganic Chemistry
Volume 2012, Article ID 989281, 9 pages
doi:10.1155/2012/989281

Research Article

Synthesis and Characterization of Nanosized Fe_2O_3 Pigments

M. F. R. Fouda,[1] M. B. El-Kholy,[1] S. A. Moustafa,[1] A. I. Hussien,[2] M. A. Wahba,[1] and M. F. El-Shahat[3]

[1] *Inorganic Chemistry Department, National Research Center, P.O. Box 12622, Dokki, Giza, Egypt*
[2] *Polymers and Pigments Department, National Research Center, P.O. Box 12622, Dokki, Giza, Egypt*
[3] *Department of Chemistry, Faculty of Science, Ain Shams University, Abbassia, Cairo 11566, Egypt*

Correspondence should be addressed to M. A. Wahba, mohamedwahba12@gmail.com

Received 10 April 2012; Accepted 17 May 2012

Academic Editor: Wolfgang Linert

The work in this paper was devoted to investigating some nanosized iron oxide pigments prepared by microemulsion technique. The role of concentration of iron salt and surfactant (cetyltrimethylammonium bromide) on the produced iron oxide was studied. The techniques employed to characterize the samples were thermogravimetric analysis, X-ray diffractometry, transmission electron microscope, infrared spectroscopy, and diffuse reflectance spectroscopy. The results revealed that the particle size of the prepared sample using 0.2 M iron sulfate and 3.2 wt% of surfactant was in the range 7–9 nm. Increasing the concentration of either iron salt or the surfactant increased the particle size of the obtained ferric oxide. The diffuse reflectance measurements showed that the charge transfer/electron pair transition absorption peak, which is closely related to the reddish color of the oxide, was shifted to a longer wavelength (blue shift) by decreasing the dimension of the particles. The samples were tested as pigments. They showed different tints of red color and were found to be promising for applications as pigments in the field of paint manufacturing.

1. Introduction

Nanostructured iron oxides are of a great interest when compared with their bulk counterpart due to their large surface area, high rate of reactivity, and due to the possibility of enhancing environmental friendly reactions. They have superior characters in nontoxicity, chemical stability, durability, and low costs [1]. Due to these properties, they find wide applications in the fields of nanoscience and nanotechnology as pigments, enhancing storage capacity in electronic recording devices, catalysts in some industries, and contrasting agents in magnetic resonance imaging [2–4].

Iron oxide nanoparticles with various structures, sizes, and morphologies have been attained. It is now well known that the morphology and size of the particles have a great impact on their chemical and physical properties. In order to control particle size and obtain monodispersed nanoparticles with a narrow size distribution, various techniques have been employed [5]. Among these techniques, water-in-oil (W/O) microemulsions or reverse micelles are particularly good reaction media for fabricating metal oxide nanoparticles. The outstanding dispersion, small particle size distribution, and shape control imparted by the microemulsion synthesis technique make it a very attractive method for synthesis of nanooxides. In this technique, nanosized water droplets are dispersed in a continuous oil medium and stabilized by surfactant molecules accumulated at the oil/water interface. These highly dispersed water droplets are ideal nanostructured reaction media for producing monodispersed nanoparticles [6]. The growth rate, shape and size of the particles produced using microemulsion technique depend on many factors such as type and concentration of surfactant [6, 7], both oil and alcohol types [8–10], speed of mixing [11], and particle aging [12].

In this paper, it is aimed to synthesize nanoparticles by application of a water-in-oil microemulsion route. The effect of changing ferric salt concentration, surfactant concentration, and calcination at different temperatures on structure, and particle size of the samples prepared by this method were discussed. The study was also directed to evaluate some of these samples as pigments and to demonstrate the effect of particle size variation on the tinting strength, hiding power,

and other physical and chemical properties of the prepared red paints.

2. Experimental

2.1. Materials. The chemicals used in the present investigation were of analytical reagent grade and obtained from Merck (Darmstadt, Germany).

2.2. Techniques. The thermogravimetric analysis was conducted using a Perkin-Elmer Delta series (TGA7) thermoanalyzer. The rate of heating was $10^{\circ}C\,min^{-1}$ in a static air. The X-ray diffractograms were recorded using the monochromatized Cu K_{α} radiation of a Bruker 8 advance diffractometer. The mean crystallite size was calculated from Scherrer formula based on the full width at half maximum intensity (FWHM) of the major peaks. The particle size and morphology of the samples were examined by a transmission electron microscope (JEOL TEM 2010) operated at 200 kV accelerating voltage. The samples were prepared by making a suspension of the powder in distilled water using ultrasonic water bath. The suspension was centrifuged for 5 min, and a drop of well-dispersed supernatant was put on a carbon grid and left to dry. The diffuse reflectance spectra were recorded using a Shimadzu UV-3101 PC-Spectrophotometer. Infrared (IR) spectroscopic analysis was conducted and recorded using a JASCO spectrometer (model FT/IR-6300 type A) in the ranges (150–650) cm^{-1} and (400–4000) cm^{-1}.

2.3. Preparation of α-Fe_2O_3 Nanoparticles. α-Fe_2O_3 nanoparticles were prepared by a microemulsion-mediated synthesis process. In this process, a first microemulsion was prepared by dissolving cetyltrimethylammonium bromide (CTAB) in n-octane, followed by the addition of heptanol. The resulted solution was stirred for 30 min until it became transparent. Next, a ferric sulfate solution was added to the microemulsion. The system was stirred slowly until a transparent microemulsion suspension was obtained. After that, a second microemulsion composed of CTAB/heptanol/octane and 0.25 M of ammonium hydroxide was prepared. Equal volumes of the two microemulsion systems were then mixed slowly while stirring. After mixing, the reverse micellar solution was vigorously stirred for 6 h keeping the pH of the system in the range of 7-8. The obtained buff precipitate was centrifuged, washed several times with deionized water and acetone, and dried at room temperature. The powders were slightly ground and calcined at 700°C for 6 h and cooled to room temperature.

The same procedures were repeated using different concentrations of ferric sulfate and CTAB surfactant to study the influence of changing concentration of the iron salt and surfactant on structure, particle size, and crystallinity of the samples.

2.4. Evaluation of the Nanoparticles as Pigments. Evaluation of the samples as pigments was carried out according to the American Society for Testing and Materials (ASTM) standard methods for evaluation of pigments. These tests included specific gravity, oil absorption, hiding power, tinting power, bleeding test, permanence to light and heat, and the chemical resistance towards acids and alkalies [13–19].

The typical heating schedules are 60 minutes at 105–120°C, 45 minutes at 120–135°C, 30 minutes at 135–150°C, 15 minutes at 150°C, and 10 minutes at 175–200°. The Alkali resistance was evaluated as Excellent: for almost no change after 60 minutes immersion; V. Good: for significant change, but no complete failure after 60 minutes immersion; Fair: for no significant change after 5-minute immersion, but complete failure after 60 minutes; Poor: for failure after immersion for 5 minutes or less. The acid resistance was evaluated as Excellent: for almost no change after 18 hours immersion; V. Good: for significant change, but no complete failure after 18-hour immersion; Fair: for no significant change after 6-hour immersion, but complete failure after 18 hours; Poor: for failure after immersion for 6 hours or less.

3. Results and Discussion

3.1. Characterizations of α-Fe_2O_3 Nanoparticles

3.1.1. Thermal Gravimetric Analysis (TGA). TGA shows three stages of weight loss in the temperature ranges: 30–160°C, 160–192°C, and 192–400°C (Figure 1). The first step: weight loss can be ascribed to desorption of physically absorbed water in the sample. The abrupt weight loss between 160°C and 400°C can be ascribed to desorption and decomposition of the surfactant and to dehydroxylation of the precipitated samples [20]. There is no further weight loss after reaching the temperature 450°C.

3.1.2. X-Ray Diffraction. The XRD patterns of the samples show well-defined peaks, which clearly indicates that the samples are crystalline (Figure 2). The diffraction patterns of the different samples showed the same characteristic peaks belonging to standard α-Fe_2O_3 phase. The Bragg lines are indexed in the hexagonal sitting of the space group R3c. The lattice parameters (*a* and *c*) of the synthesized powder were determined using the least square fits. Both the diffraction peaks and lattice parameters of the samples were found to be in a good agreement with those reported for hematite in the literature (JCPDS Card no. 89-0529) [21]. Moreover, it was found that the ratio between the integrated intensities of (104) to (110) peaks (I_{104}/I_{110}) is greater than the unity which corresponds well to the standard XRD pattern of hematite [22].

It was observed that the gradual increase in the concentration of the ferric salt led to an increase in the relative intensity of the peaks indicating the improvement of crystallinity. Full-width at half-maximum (FWHM) data was used to calculate the average crystallite size for each sample in its respective X-ray diffractogram using the Scherrer's equation [23] (Table 1). The microstrain was estimated by analyzing the X-ray diffraction lines using Williamson and Hall method. It was observed that the integral breadth of the Bragg lines of the 0.2 M assisted sample was slightly

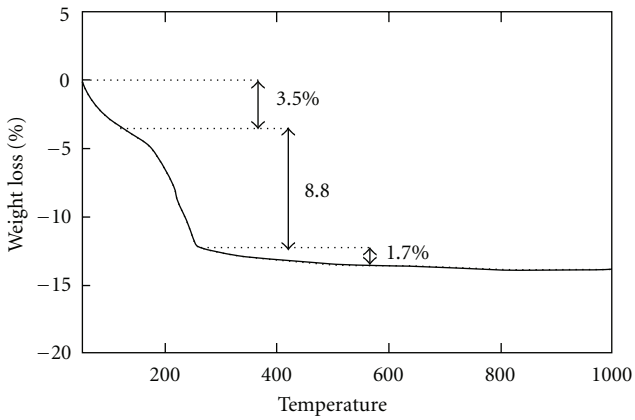

Figure 1: TGA pattern of the as-synthesized sample assisted by 0.2 M ferric sulfate.

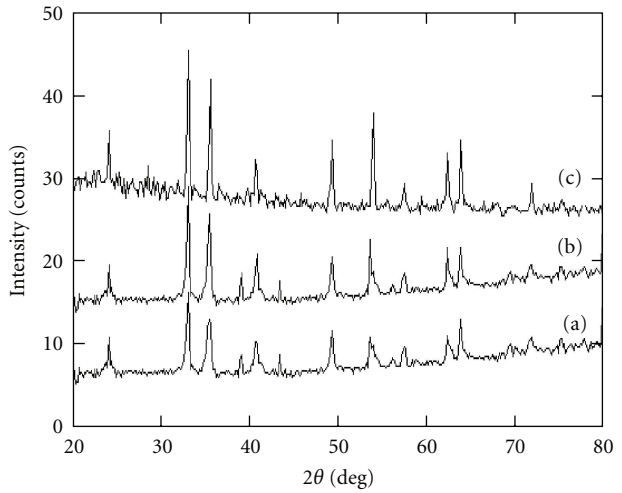

Figure 2: XRD pattern of α-Fe_2O_3 powder synthesized by microemulsion method using different molar concentrations of Ferric sulfate: (a) 0.2 M, (b) 0.4 M, and (c) 0.6 M.

greater than that of the 0.4 and 0.6 M samples, respectively. This suggests that it has a smaller grain size and higher microstrain content (see Table 1). These results were found to be in accordance with those reported in the literature referring that large-sized crystals possess small-lattice strain while small-sized crystals possess high-lattice strain [24, 25].

3.1.3. Transmission Electron Microscope. Figures 3(a)—3(c) represent TEM images of α-Fe_2O_3 samples prepared using different molar concentrations of ferric sulfate. They showed that the particles are nearly spherical and lie in the nanosized range. They show also a narrow-particle-size variation throughout the field of the micrograph.

This can be ascribed to that the quaternary system composed of CTAB/n-heptanol/n-octane/water which was used as the reaction medium resulted in the formation of nanosized water droplets dispersed in the continuous oil medium and stabilized by the surfactant molecules. These droplets were used as nanoreactors to carry out chemical

Table 1: X-ray data of the α-Fe_2O_3 samples synthesized. Using different molar concentrations of ferric sulfate.

Molar conc.	aÅ	cÅ	vÅ^3	Average crystallite size/nm	
				XRD	TEM
0.2 M	5.03(2)	13.74(3)	301.3	10	7–9
0.4 M	5.03(7)	13.74(1)	301.9	13	12–16
0.6 M	5.03(5)	13.73(9)	301.6	18	16–22

reactions in their restricted geometries and to limit the growth of α-Fe_2O_3 particles and render particle size in the nanometer scale [26].

TEM images revealed also that the particle size increased by using high concentrations of the iron salt. It was found to be in the range 7–9 nm for the α-Fe_2O_3 sample synthesized using 0.2 M of ferric sulfate, while it varied between 12–16 nm and 16–22 nm for the prepared samples using 0.40 and 0.60 molar concentrations of the salt, respectively. These findings may be attributed to that when the concentration of the iron salt increased from 0.20 to 0.60 M, a higher micellar uptake of the α-Fe_2O_3 nanoparticles has occurred and this led to an increase in the ferric ion occupancy number per reverse micelle. Subsequently, the nucleation growth was enhanced and the particle size increased [27, 28].

3.1.4. Infrared Spectra. Infrared spectroscopy has been carried out to characterize the composition of the as-prepared samples. It also studied the vibration of oxygen atoms around the metal atom in the bulk of ferric oxide lattice.

(a) *Infrared Spectra (Middle Region 400–4000 cm^{-1}).* The infrared spectra of the as-synthesized precursor samples before thermal treatment at 700°C (Figure 4(a)) show a strong wide band in the region 3000–3660 cm^{-1} and a moderate band around 1650 cm^{-1}. These bands are assigned to adsorbed water and vibration of the OH groups, respectively, (Figure 4) [29]. They showed also absorption bands at around 2920, 2850, 1510, 1330, and 1470 cm^{-1} which may be attributed to the organic residuals of oil, alcohol, and surfactant [30].

Figure 4(b) showed that almost all the bands vanished when the dried iron oxide containing precursors were heated at 700°C. Most of the absorption bands have disappeared due to the complete thermal decomposition of the organic residues at 700°C. Although the O–H bond vibration around 3000 cm^{-1} is still present, the intensity of this band decreased markedly on heating the samples at 700°C. The bands which are related to FeO_6 structure of the samples will be discussed next in the far region infrared spectra.

(b) *Infrared Spectra (Far Region 150–650 cm^{-1}).* As expected from the factor group analysis, the spectra of the samples following dry-thermal treatment at 700°C (Figure 5) displayed two distinct infrared modes, that is, $2A_{2u}+3E_u$. The observed five bands were in a good agreement with the prediction of the factor group analysis of the hexagonal structure of

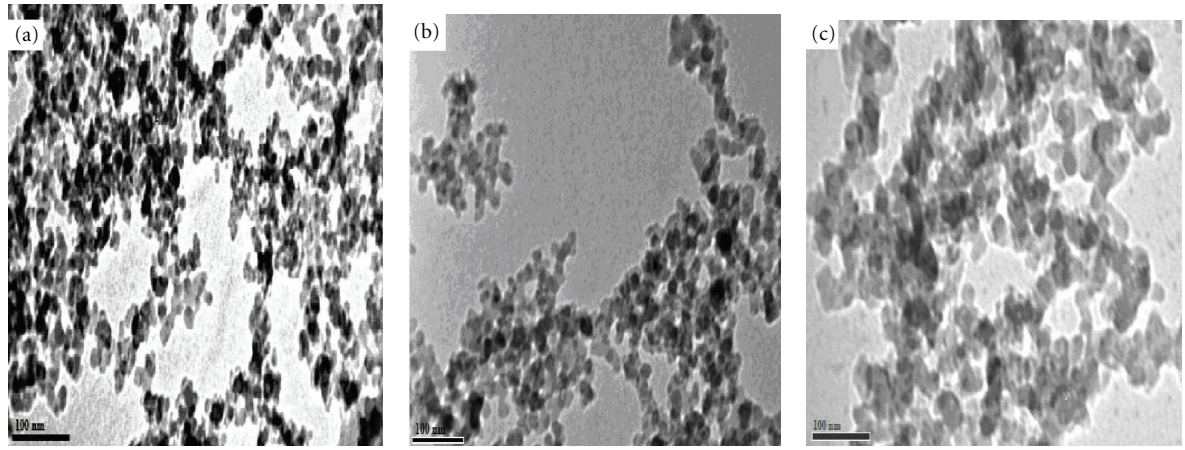

Figure 3: TEM morphologies of the α-Fe_2O_3 sample synthesized by microemulsion method using (a) 0.2, (b) 0.4 M, and (c) 0.6 ferric sulfate.

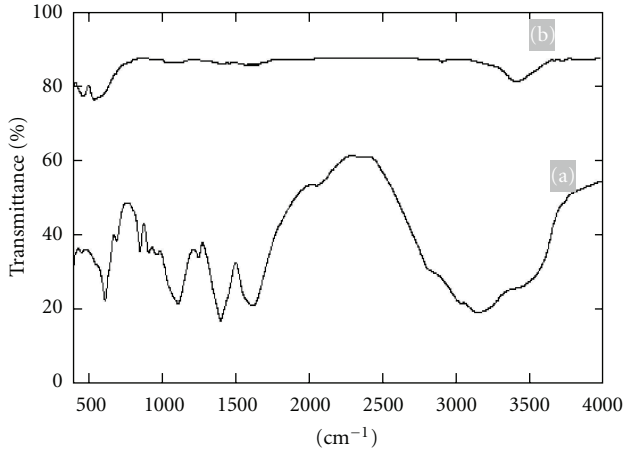

Figure 4: Mid-IR spectra of as-synthesized samples by microemulsion method using $Fe_2(SO_4)_3$ (a) before calcination and (b) after calcination 700°C.

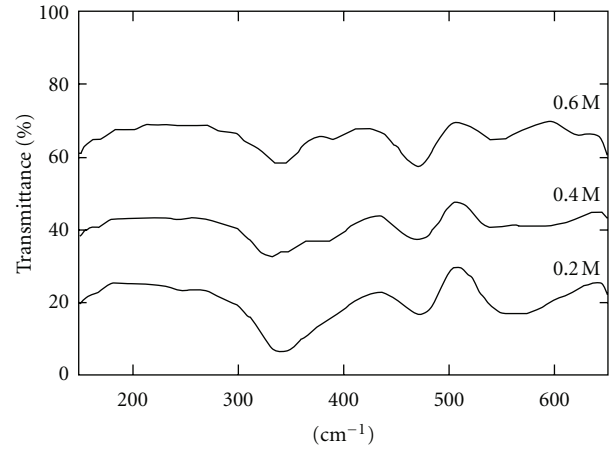

Figure 5: Far-IR spectra of α-Fe_2O_3 prepared by microemulsion method using 0.2, 0.4, and 0.6 M concentrations of $Fe_2(SO_4)_3$ and calcined at 700°C.

hematite [31]. The two bands observed in the ranges 384–388 cm^{-1} and at 625 cm^{-1} were attributed to two one-dimensional A_{2u} vibration modes with polarization parallel to c-axis of the hematite crystal, while the bands observed in the ranges (329–337) cm^{-1}, (470–473) cm^{-1}, and (552–558) cm^{-1} are related to E_u vibration mode with polarization perpendicular to the c-axis [32].

The factor group analysis claimed that hematite has another band in the low wavenumber region (E_u symmetry) at 230 cm^{-1} which was not recognized in our samples [33, 34]. The disappearance of one band around 230 cm^{-1} in all samples; two bands around 385 and 625 cm^{-1} for the sample synthesized using 0.20 M of ferric sulfate; one band around 625 cm^{-1} for the 0.40 M sample may be ascribed to the small particle size of the prepared α-Fe_2O_3 nanoparticles [32].

3.1.5. Diffuse Reflectance Spectra. The diffuse reflectance spectra of the synthesized α-Fe_2O_3 samples are shown in Figure 6. The red color of the prepared samples can be assigned to the ligand-to-metal charge transfer (CT) transition: the $^6t_{1u}$ (O_2^-) → $^2t_{2g}$ (Fe^{3+}) which appeared in the range 555–561 nm [33]. A second specificity of the samples is the spin and parity forbidden d-d transitions [34]. Four d-d transition bands characteristic α-Fe_2O_3 were observed in the visible to near IR region. In the light of the ligand field theory, the three bands observed in the ranges (429–433) nm, (668–672) nm, and (875–877) nm are assigned to the following ligand field transitions: $^6A_1 \rightarrow {}^4E$; $^4A_1$, $^6A_1 \rightarrow {}^4T_2$, and $^6A_1 \rightarrow {}^4A_l$, respectively. The position of the fourth band, assigned to the electron pair transition "EPT" $^6A_1 + {}^6A_1 \rightarrow ({}^4T_1 + {}^4T_1)$ double excitation, overlapped with the position of the CT band in the range (555–561) nm. The band position at (555–561) nm together with the band at (875–877) nm indicated that the prepared samples are red iron oxide, hematite [35]. The position of the CT/EPT band in the α-Fe_2O_3 sample synthesized using 0.2 M of iron

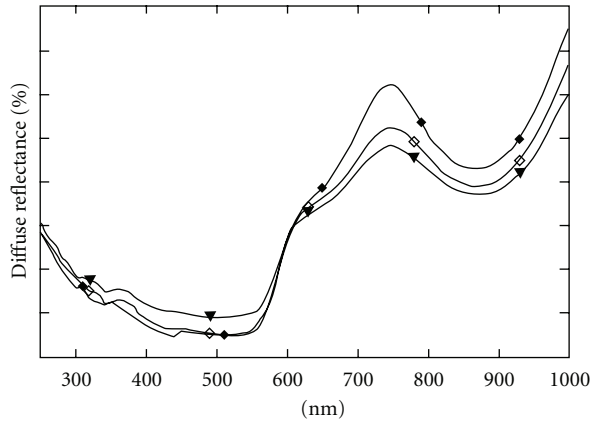

Figure 6: Diffuse reflectance spectra of α-Fe_2O_3 prepared by microemulsion method using (►) 0.2 M, (□) 0.4 M, and (♦) 0.6 M concentrations of $Fe_2(SO_4)_3$ and calcined at 700°C.

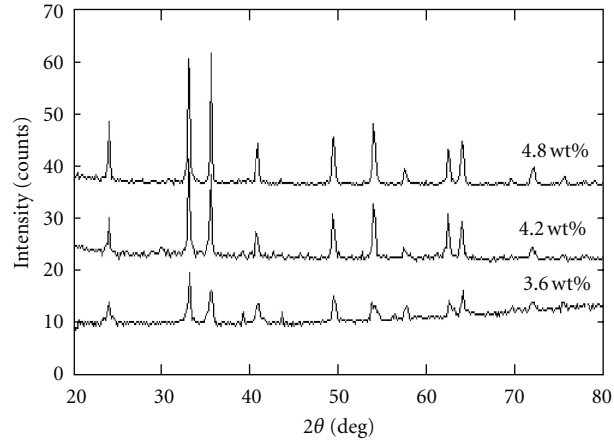

Figure 7: XRD pattern of α-Fe_2O_3 powder synthesized by microemulsion method using different concentration of surfactant (CTAB).

sulfate was shifted to a longer wavelength (blue shift) than in the samples prepared using 0.4 and 0.6 M of the ferric salt, respectively. This can be ascribed to the smaller particle size of the 0.2 M sample. Another property that can be ascribed to the small particle size of 0.2 M sample is its higher reflectance in the red color range than the 0.4 and 0.6 M samples, respectively [35].

3.2. Effect of Changing Surfactant Concentration

3.2.1. X-Ray Diffraction. The XRD patterns of α-Fe_2O_3 powders synthesized using different surfactant concentration values are displayed in Figure 7. The diffraction patterns of the samples matched perfectly with the standard α-Fe_2O_3 (XRD Card no. 89-0529). The X-ray diffractograms showed also that the diffraction peaks became stronger and sharper as the concentration of surfactant increased. This indicated improving of crystallinity and increasing of the particle size. The average crystal size was estimated by analyzing X-ray diffraction lines using Scherrer formula and Williamson and Hall method, respectively (Table 2).

3.2.2. Transmission Electron Microscope. Figures 8(a)—8(c) represent the transmission electron micrographs prepared using different concentration of CTAB surfactant. It was observed that elevating surfactant concentration resulted in an increase in the particle size (Table 2). This observation can be explained by that increasing surfactant concentration at constant water content resulted in an increase in the number of the reaction pools (water in oil droplets). Consequently, more sites are available for nucleation of the particles, which are expected to yield smaller particles [36]. However, the increased number of droplets, resulted from increasing the concentration of the surfactant, that led to a high rate of collisions among these droplets (shorter droplet mean-free path), hence, increased the probability of agglomeration of nanoparticles upon centrifugal separation. In other words, the monodispersed particles suspended in a microemulsion resulted in more agglomeration upon settling down and drying. Similar trends were reported in the literature for nanoparticle synthesis by microemulsion technique [37].

Table 2: X-ray data of α-Fe_2O_3 samples synthesized using different concentration of CTAB surfactant.

CTAB conc. (wt%)	aÅ	cÅ	vÅ^3	Average crystallite size (nm)
3.5	5.03(2)	13.740(9)	301.3	10
4.2	5.03(7)	13.74(1)	301.9	13
4.8	5.03(5)	13.73(9)	301.6	23

3.3. Effect of Changing Calcination Temperature. Figure 9 shows a series of XRD patterns of different iron oxide samples produced at various temperatures ranging from 200 to 700°C. The XRD patterns showed that the crystalline phase started to appear on calcination of the parent material at ≥400°C. This finding is supported by the TGA analysis (see Figure 1). When the temperature was not high enough to break down the surfactant, below 300°C, the observed X-ray diffraction peaks were found to be smooth and undefined. On the other hand, when the calcination temperature was raised to 400°C, the surfactant decomposed and the XRD peaks appeared as weak broad peaks. The presence of these broad peaks indicated the small (nanosize) crystallite size of the formed product at this temperature. By raising calcination temperature, the peaks corresponding to goethite and ferrihydrite phases disappeared, while those corresponding to α-Fe_2O_3 phase became predominant. When the temperature reached 500°C, the XRD pattern of the sample agreed well with the standard α-Fe_2O_3 perfectly, indicating the end of phase transformation. Further calcination of the powder improved the crystallinity of the products but did not cause any changes in phase composition.

3.4. Assessment of Some α-Fe_2O_3 Samples as Pigments. Evaluation of some samples as pigments was carried out according to the ASTM standard methods for evaluation of pigments

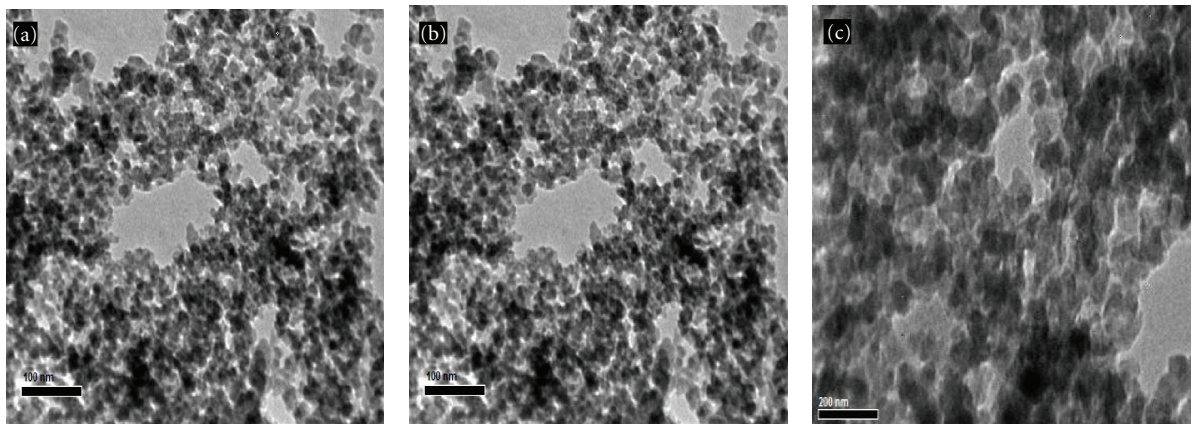

(a) (b) (c)

Figure 8: TEM morphologies of the α-Fe_2O_3 sample synthesized by microemulsion method using (a) 3.6, (b) 4.2, and (c) 4.8 wt % of surfactant.

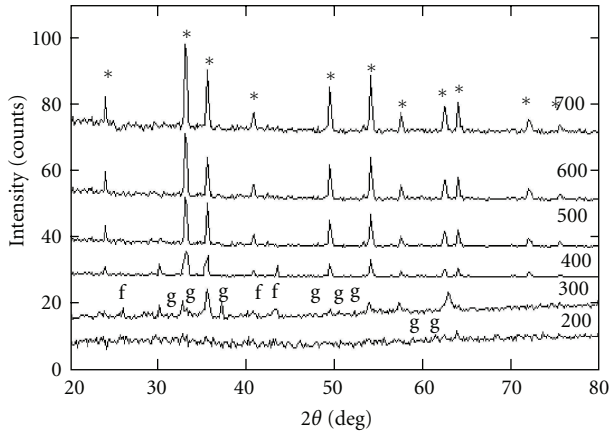

Figure 9: X-ray powder diffractograms for iron oxide particles prepared by microemulsion method and calcined at different temperatures (200–700°C) g (goethite), f (ferrihydrite), and * (hematite).

(Table 3). It was found that the specific gravity values of the samples were in the range between 4.99 and 5.16. These values are considered moderate values of specific gravity and make the prepared α-Fe_2O_3 nanoparticles suitable for application as pigments since high specific gravity values lead to settling of pigments in preparation of paint formulations. The calculated oil absorption values of the samples were found to be low. This leads to a reduction in the paint costs due to the small amount of oil needed to convert the as-prepared pigments to their corresponding paints.

The prepared samples showed high degrees of tinting. It was found also that the tinting strength of the synthesized nanosized pigments, which is defined as the ability of a pigment to influence the color of a dispersion containing other pigments, was improved as the particle size decreased. The paint film formed using 0.20 M of the iron salt showed the highest tinting power followed by those prepared using 0.40 and 0.60 M of the iron salt, respectively (Figure 10). This is assigned to that the scattering efficiency of the film increased as the particle size decreased. The samples showed also a high level of hiding power. Therefore they are capable of producing finished films whose opacity using a low concentration of the pigment is equivalent to that normally observed using higher concentration when using a coarser material. Similarly, the hiding power was enhanced as the particle size decreased. This is related to the increased probability that light entering the applied film will be reflected away from the substrate, hence effectively hiding it from view.

The prepared pigments are all distinct for their excellent bleed resistance against various solvents such as water, ethanol, acetone, chloroform, carbon tetrachloride, toluene, xylene, and tetrahydrofuran. They showed also excellent resistance towards acids and alkalies such as 5% H_2SO_4, 2% NaOH, and 5% Na_2CO_3, whereas they showed very good resistance towards 5% HCl and saturated solution of $Ca(OH)_2$. Moreover, they revealed excellent resistance toward light and heat. This can be ascribed to the ability of these pigments, due to their small- and narrow-size distribution, to be well packed within the coating film surface. This property resulted in the formation of uniform surface finish. The surface uniformity in combination with the high scattering power associated with small particle size resulted in a high degree of gloss that is a desirable outcome for many applications. The small particle size also improved the weathering characteristics of coatings since large particles or agglomerates can be more easily dislodged from the coating, resulting in that the film surface rapidly loses its gloss. Overall, the good physical and chemical properties of the prepared samples showed that these compounds can be used satisfactorily as suitable pigments for coating applications.

4. Conclusion

α-Fe_2O_3 nanoparticles were successfully synthesized using varying concentrations of iron sulfate and cetyltrimethylammonium bromide surfactant (CTAB). The size of the

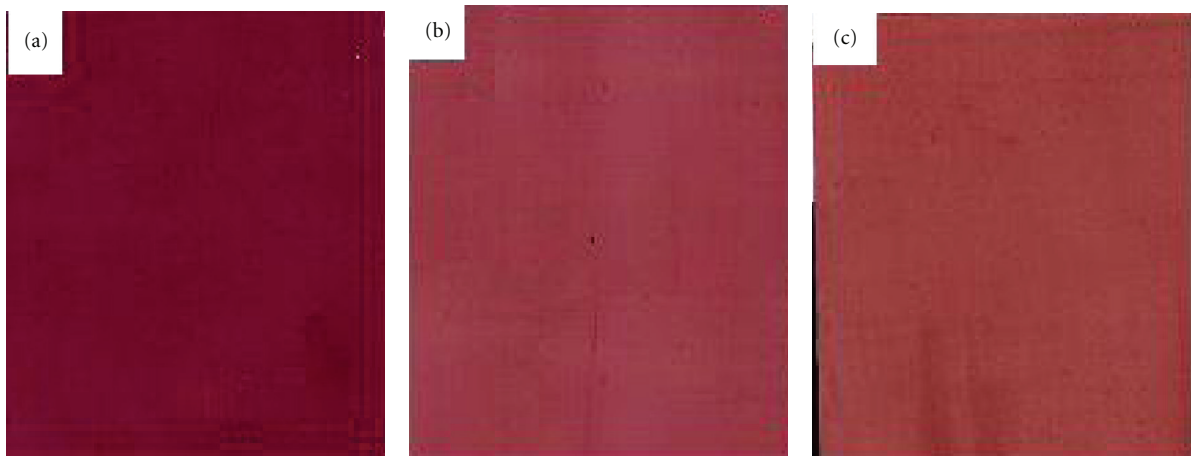

Figure 10: Tinting power of the α-Fe_2O_3 pigments prepared using (a) 0.2 M, (b) 0.4 M, and (c) 0.6 M of ferric sulfate.

Table 3: Physical and chemical properties of α-Fe_2O_3 nanoparticles prepared using microemulsion method.

Physical and chemical properties	Fe_2O_3 pigment prepared using		
	0.2 M $Fe_2(SO_4)_3$	0.4 M $Fe_2(SO_4)_3$	0.6 M $Fe_2(SO_4)_3$
Average particles size	9	14	19
Sp. Gr.	5.16	5.1	4.99
Solubility	Insoluble	Insoluble	Insoluble
Oil abs.	27	26	24
Hiding power	4.5	4.3	4.1
Resistance against heating at (700°C)	Excellent	Excellent	Excellent
Fastness properties against			
Sulfuric acid 5%	Excellent	Excellent	Excellent
Hydrochloric acid 5%	V. Good	V. Good	V. Good
Sod. Hyroxide, 2%	Excellent	Excellent	Excellent
Sod, Carbonate, 5%	Excellent	Excellent	Excellent
Cal. Hydroxide (Saturated Solution)	V. Good	V. Good	V. Good
Organic Solvents*	Insoluble	Insoluble	Insoluble
Linseed Oil	Insoluble	Insoluble	Insoluble
Oleic Acid	Insoluble	Insoluble	Insoluble

* Water, ethanol, acetone, chloroform, carbon tetrachloride, toluene, xylene, and tetrahydrofuran.

particles was found to increase using high concentrations of the iron salt or the surfactant. Using elevated concentration of the iron salt resulted in an increase in the ferric ion occupancy number per reverse micelle and an increase in the ionic strength of the water pool. Subsequently, the nucleation growth improved and the particle size increased. On the other hand, raising surfactant concentration increased concentration of water in oil droplets. This led to a high rate of collisions among these droplets (shorter droplet mean-free path), hence, increased probability of agglomeration of nanoparticles upon centrifugal separation.

The prepared samples demonstrated good pigments properties showing that these compounds can be used satisfactorily for coating applications. The α-Fe_2O_3 sample synthesized using 0.20 M of the ferric salt showed the best pigment properties. This can be ascribed to its higher scattering, reflection efficiency, and well-packing at the film surface which is related to its small particle size; it displayed the highest tinting and hiding powers followed by the samples prepared using 0.40 and 0.60 M of the salt, respectively.

Acknowledgment

The financial support from the National Research Center of Egypt is gratefully acknowledged.

References

[1] M. A. Legodi and D. de Waal, "The preparation of magnetite, goethite, hematite and maghemite of pigment quality from mill scale iron waste," *Dyes and Pigments*, vol. 74, no. 1, pp. 161–168, 2007.

[2] Y. Sasaki, N. Usuki, K. Matsuo, and M. Kishimoto, "Development of NanoCAP technology for high-density recording," *IEEE Transactions on Magnetics*, vol. 41, no. 10, pp. 3241–3243, 2005.

[3] M. Azhar Uddin, H. Tsuda, S. Wu, and E. Sasaoka, "Catalytic decomposition of biomass tars with iron oxide catalysts," *Fuel*, vol. 87, no. 4-5, pp. 451–459, 2008.

[4] M. Matsuoka, Y. Nakatani, and H. Ohido, "γ-Fe_2O_3 ceramic gas sensor," Matsushita National Technical Report 24, 1978, 461–473.

[5] B. L. Cushing, V. L. Kolesnichenko, and C. J. O'Connor, "Recent advances in the liquid-phase syntheses of inorganic nanoparticles," *Chemical Reviews*, vol. 104, no. 9, pp. 3893–3946, 2004.

[6] I. Lisiecki and M. P. Pileni, "Synthesis of copper metallic clusters using reverse micelles as microreactors," *Journal of the American Chemical Society*, vol. 115, no. 10, pp. 3887–3896, 1993.

[7] P. S. Shah, J. D. Holmes, K. P. Johnston, and B. A. Korgel, "Size-selective dispersion of dodecanethiol-coated nanocrystals in liquid and supereritical ethane by density tuning," *Journal of Physical Chemistry B*, vol. 106, no. 10, pp. 2545–2551, 2002.

[8] M. Summers, J. Eastoe, and S. Davis, "Formation of $BaSO_4$ nanoparticles in microemulsions with polymerized surfactant shells," *Langmuir*, vol. 18, no. 12, pp. 5023–5026, 2002.

[9] K. E. Marchand, M. Tarret, J. P. Lechaire, L. Normand, S. Kasztelan, and T. Cseri, "Investigation of AOT-based microemulsions for the controlled synthesis of MoSx nanoparticles: an electron microscopy study," *Colloids and Surfaces A*, vol. 214, no. 1–3, pp. 239–248, 2003.

[10] F. Porta, L. Prati, M. Rossi, and G. Scari, "Synthesis of Au(0) nanoparticles from W/O microemulsions," *Colloids and Surfaces A*, vol. 211, no. 1, pp. 43–48, 2002.

[11] J. Singh, M. Srivastava, J. Dutta, and P. K. Dutta, "Preparation and properties of hybrid monodispersed magnetic α-Fe_2O_3 based chitosan nanocomposite film for industrial and biomedical applications," *International Journal of Biological Macromolecules*, vol. 48, no. 1, pp. 170–176, 2011.

[12] A. R. Loukanov, C. D. Dushkin, K. I. Papazova, A. V. Kirov, M. V. Abrashev, and E. Adachi, "Photoluminescence depending on the ZnS shell thickness of CdS/ZnS core-shell semiconductor nanoparticles," *Colloids and Surfaces A*, vol. 245, no. 1–3, pp. 9–14, 2004.

[13] ASTM, "Standard test methods for specific gravity of pigments ASTM," Tech. Rep. D153, 2008.

[14] ASTM, "Standard test method for effect of household chemicals on clear and pigmented organic finishes," Tech. Rep. D1308, 1987.

[15] ASTM, "Standard test method for oil absorption of pigments by spatula rub-out," Tech. Rep. D281, 1995.

[16] ASTM, "Standard Test Methods for Bleeding of Pigments," Tech. Rep. D279, 1987.

[17] ASTM, "Standard test methods for resistance of dried films of varnishes to water and alkali," Tech. Rep. D1647, 1989.

[18] ASTM, "Standard test method for color and strength of chromatic pigments with a mechanical muller," Tech. Rep. D387, 2000.

[19] ASTM, "Standard test method for acid and mortar resistance of factory-applied clear coatings on extruded aluminum products," Tech. Rep. D3260, 2001.

[20] B. Nikoobakht and M. A. El-Sayed, "Evidence for bilayer assembly of cationic surfactants on the surface of gold nanorods," *Langmuir*, vol. 17, no. 20, pp. 6368–6374, 2001.

[21] V. A. Sadykov, L. A. Isupova, S. V. Tsybulya et al., "Effect of mechanical activation on the real structure and reactivity of iron (III) oxide with corundum-type structure," *Journal of Solid State Chemistry*, vol. 123, no. 2, pp. 191–202, 1996.

[22] H. Fan, B. Song, J. Liu, Z. Yang, and Q. Li, "Thermal formation mechanism and size control of spherical hematite nanoparticles," *Materials Chemistry and Physics*, vol. 89, no. 2-3, pp. 321–325, 2005.

[23] M. Boutonnet, J. Kizling, V. Mintsa-Eya et al., "Monodisperse colloidal metal particles from nonaqueous solutions: catalytic behavior in hydrogenation of but-1-ene of platinum, palladium, and rhodium particles supported on pumice," *Journal of Catalysis*, vol. 103, no. 1, pp. 95–104, 1987.

[24] S. Palaniandy and N. H. Jamil, "Influence of milling conditions on the mechanochemical synthesis of CaTiO3 nanoparticles," *Journal of Alloys and Compounds*, vol. 476, no. 1-2, pp. 894–902, 2009.

[25] D. Chaira, B. K. Mishra, and S. Sangal, "Efficient synthesis and characterization of iron carbide powder by reaction milling," *Powder Technology*, vol. 191, no. 1-2, pp. 149–154, 2009.

[26] R. A. West, *Solid State Chemistry and Its Applications*, vol. 172, John Wiley & Sons, New York, NY, USA, 1985.

[27] J. H. Adair, T. Li, T. Kido et al., "Recent developments in the preparation and properties of nanometer-size spherical and platelet-shaped particles and composite particles," *Materials Science and Engineering R*, vol. 23, no. 4-5, pp. 139–242, 1998.

[28] M. P. Pileni, "Water in oil colloïdal droplets used as microreactors," *Advances in Colloid and Interface Science*, vol. 46, pp. 139–163, 1993.

[29] D. M. Fernandes, A. A. W. Hechenleitner, M. F. Silva et al., "Preparation and characterization of NiO, Fe_2O_3, $Ni_{0.04}Zn_{0.96O}$ and $Fe_{0.03}Zn_{0.97O}$ nanoparticles," *Materials Chemistry and Physics*, vol. 118, no. 2-3, pp. 447–452, 2009.

[30] J. Huang, H. Zhuang, and W. Li, "Synthesis and characterization of nano crystalline BaFe12O19 powders by low temperature combustion," *Materials Research Bulletin*, vol. 38, no. 1, pp. 149–159, 2003.

[31] A. M. Jubb and H. C. Allen, "Vibrational spectroscopic characterization of hematite, maghemite, and magnetite thin films produced by vapor deposition," *ACS Applied Materials and Interfaces*, vol. 2, no. 10, pp. 2804–2812, 2010.

[32] J. L. Rendon and C. J. Serna, "IR spectra of powder hematite: effects of particle size and shape," *Clay Minerals*, vol. 16, no. 4, pp. 375–382, 1981.

[33] N. Pailhe, A. Wattiaux, M. Gaudon, and A. Demourgues, "Water in oil colloïdal droplets used as microreactors," *Journal of Solid State Chemistry*, vol. 181, pp. 1040–1047, 2008.

[34] M. Elias, C. Chartier, G. Prévot, H. Garay, and C. Vignaud, "The colour of ochres explained by their composition," *Materials Science and Engineering B*, vol. 127, no. 1, pp. 70–80, 2006.

[35] D. M. Sherman and T. D. Waite, "Electronic spectra of Fe^{3+} oxides and oxide hydroxides in the near IR to near UV," *American Mineralogist*, vol. 70, no. 11-12, pp. 1262–1269, 1985.

[36] M. R. Cornell and U. Schwertmann, *The Iron Oxides: Structure, Properties, Reactions, Occurrences and Uses*, Wiley-VCH, Weinheim, Germany, 2nd ed edition, 2003.

[37] E. McEvoy, A. Marsh, K. Altria, S. Donegan, and J. Power, "Recent advances in the development and application of microemulsion EKC," *Electrophoresis*, vol. 28, no. 1-2, pp. 193–207, 2007.